PHYSICAL REVIEW RESEARCH **2**, 013176 (2020)

Electric field driven reconfigurable multistable topological defect patterns

Saša Harkai,[1] Bryce S. Murray,[2] Charles Rosenblatt,[2,*] and Samo Kralj[1,3,*]
[1]*Condensed Matter Physics, Jožef Stefan Institute, SI-1000 Ljubljana, Slovenia*
[2]*Department of Physics, Case Western Reserve University Cleveland, Ohio 44106, USA*
[3]*Department of Physics, Faculty of Natural Sciences and Mathematics, University of Maribor, SI-2000 Maribor, Slovenia*

(Received 11 December 2019; accepted 21 January 2020; published 20 February 2020)

Topological defects appear in symmetry breaking phase transitions and are ubiquitous throughout Nature. As an ideal testbed for their study, defect configurations in nematic liquid crystals (NLCs) could be exploited in a rich variety of technological applications. Here we report on robust theoretical and experimental investigations in which an external electric field is used to switch between predetermined stable chargeless disclination patterns in a nematic cell, where the cell is sufficiently thick that the disclinations start and terminate at the same surface. The different defect configurations are stabilized by a master substrate that enforces a lattice of surface defects exhibiting zero total topological charge value. Theoretically, we model disclination configurations using a Landau-de Gennes phenomenological model. Experimentally, we enable diverse defect patterns by implementing an in-house-developed atomic force measurement scribing method, where NLC configurations are monitored via polarized optical microscopy. We show numerically and experimentally that an "alphabet" of up to 18 unique line defect configurations can be stabilized in a 4 × 4 lattice of alternating $s = \pm 1$ surface defects, which can be "rewired" multistably using appropriate field manipulation. Our proof-of-concept mechanism may lead to a variety of applications, such as multistable optical displays and rewirable nanowires. Our studies also are of interest from a fundamental perspective. We demonstrate that a chargeless line could simultaneously exhibit defect-antidefect properties. Consequently, a pair of such antiparallel disclinations exhibits an attractive interaction. For a sufficiently closely spaced pair of substrate-pinned defects, this interaction could trigger rewiring, or annihilation if defects are depinned.

DOI: 10.1103/PhysRevResearch.2.013176

I. INTRODUCTION

Topological defects (TDs), in which the relevant order parameter field becomes ill-defined at a point, line, or surface [1], appear as a consequence of symmetry-breaking phase transitions. Since these structures generate complex order parameter patterns, TDs are of interest throughout the physical sciences, spanning such diverse areas as condensed materials [2–5] and cosmology [6], with TD-dominated physical properties exhibiting universal behavior independent of the systems' microscopic details [1].

Owing to their large response to external stimuli and large optical and electric anisotropies, liquid crystals [7] (LCs) provide an ideal test bed for many topological-based phenomena and motivate manipulation of TDs over a wide range of scientifically important systems, such as superfluid vortices [8,9] in ^{3}He and ^{4}He, Bose-Einstein condensates [10], and Abrikosov vortices in superconductors [11]. Furthermore, TDs in liquid crystals could be exploited in various technological applications. For example, they can strongly impact LC optical properties [7]; generate optical vortices [12]; and efficiently trap appropriate (surface decorated) nano [13–16] or colloidal particles [17,18], which could lead to development of tunable metamaterials, rewirable nano or micro-wires, and self-healing materials.

The nematic phase represents the simplest LC phase [7]. The conventional uniaxial nematic LC phase is a fluid consisting of rodlike molecules. Local ordering is commonly determined by the unit vector field $\boldsymbol{n}$, referred to as the nematic "director" field, where $\pm\boldsymbol{n}$ states are equivalent in bulk; this corresponds to quadrupolar symmetry of the director. In equilibrium there is long range orientational order, with $\boldsymbol{n}$ being spatially uniform along a symmetry breaking direction. Common excitations in $\boldsymbol{n}$ are line defects (disclinations) corresponding to noncontractible loops in the order parameter space characterized by the "winding number" s, in which $\boldsymbol{n}$ rotates s times as one circumnavigates the defect core. In two dimensions (2D), defects are characterized by half-integer or integer values of s, where different values of s correspond to topologically different structures. On the other hand, in 3D, only $s = \pm 1/2$ defects exist [19,20] (i.e., $+\boldsymbol{n}$ rotates to $-\boldsymbol{n}$ as one encircles a line defect) where states $s = -1/2$ and $s = +1/2$ are topologically equivalent. Their impact on the director's far-field is determined by the total topological "charge" q, defined by noncontractible spheres enclosing the entire line defect. We refer to line defects with $q = 0$ and $q \neq 0$ as *chargeless* and *charged* TDs, respectively.

---

[*] Corresponding authors: samo.kralj@um.si; rosenblatt@case.edu

Isolated chargeless loops tend to vanish over time. Note that for ferromagnetic (dipolar) order, as opposed to nematic (quadrupolar) order, line defects are not topologically protected—they can escape along the third dimension [21] via reorientation of the order parameter—owing to the ferromagnet's dipolar order parameter field. Thus a ferromagnet's winding number s must be an integer.

There are strong motivations to stabilize and manipulate diverse complex lattices of nematic line defects, for both fundamental and application reasons. They could be stabilized by chirality [7,22], dispersed colloids [23,24], or confining surface treatments [17,25]. However, *in situ* manipulation of TDs is notoriously difficult. Moreover, their controllable and multistable manipulation among predetermined configurations is scarce [17,23,26], and in particular, has been totally unexplored for ubiquitous "chargeless" defect lines [5]. For purposes of this paper we focus on work presented in Refs. [25,27–29]. References [25], [27], and [28] illustrate different methods for enforcing a regular array of topological defects of alternating winding number. These include an atomic force microscope scribing method [25], a plasmonic photoalignment technique [27], or combining doped ions and polymer alignment layers [28]. For controlled switching, one can imagine the use of laser tweezers [5,23], a slow technique that would need to be utilized serially, from one defect to another. Interdigitated electrodes [29] have been used for efficient robust switching among multistable nematic director patterns, although not for the control of disclination lines. Our approach of a simple, spatially homogeneous electric field and patterned defect arrays facilitates rapid rewiring of defects.

Here we demonstrate the systematic assembly and reassembly of a lattice of chargeless line defects [see Fig. 1(a)] in a thin nematic liquid crystal cell that is nanopatterned for orientational order. We report on a robust theoretical framework and corresponding experimental results in which an external electric field is used to switch between predetermined and stable line defect configurations by coupling the field to the complex director profile surrounding the defects. We anticipate that our proof-of-concept for "rewiring" topological line defects in liquid crystals also may lead to a variety of applications based on reconfigurable nanowires in soft matrices such as multistable optical displays, electronics, and charge carrier pathways for photovoltaics.

The plan paper of the paper is as follows. In Sec. II, we present the geometry and topology that enables a rich diversity of multi-stable nematic chargeless disclinations in our numerical and experimental research. In Sec. III, a Landau-de Gennes phenomenological model in terms of the nematic tensor order parameter is introduced. The experimental setup is described in Sec. IV. In Sec. V, numerical results are reported, in which we show multistability of defect configurations and some representative external electric field driven disclination rewirings. Experimental confirmation of proof-of-concept for the rewiring mechanism proposed numerically is presented in Sec. VI. In the last section, we summarize results. Some technical details are assembled in Appendix.

II. GEOMETRY OF THE PROBLEM

Our investigations examine electric field driven transformations of lattices of line defect segments in a nematic liquid crystal confined to a plane-parallel cell. Key geometrical and topological features of the cell used in the main numerical and experimental studies are sketched schematically in Fig. 2. We stabilize patterns of TDs in the LC by means of controlled boundary conditions, i.e., we enforce the topology at the substrates [25]. In terms of Cartesian coordinates (x,y,z), defined by the unit vector triad $(\boldsymbol{e}_x, \boldsymbol{e}_y, \boldsymbol{e}_z)$, the bottom *master* and the top *slave* planar-aligning substrates are placed at $z = 0$ and $z = h$ [Fig. 2(a)], respectively. The master substrate was patterned with a square array of enforced topological defects each having strength $s = \pm 1$ [see Fig. 2(b)] and defined by the equation

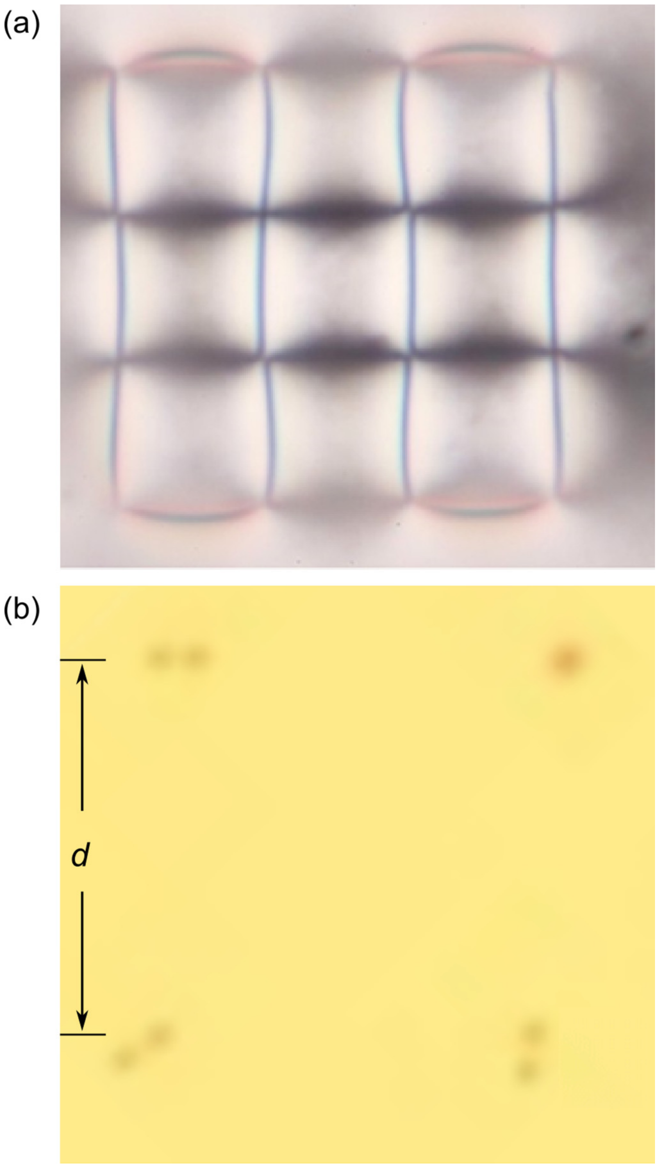

FIG. 1. Nematic LC cell with line defects. (a) Experimental polarizing microscopy texture of a nematic LC cell exhibiting line defects confined near the master plate. (b) Bright field image of a section of the sample showing three of the four integer $s = \pm 1$ defects having decomposed into half-integer defects.

$$\phi(x, y) = \sum_{k=1}^{N} s_k \arctan\left(\frac{y - y_k}{x - x_k}\right) + \phi_0. \tag{1}$$

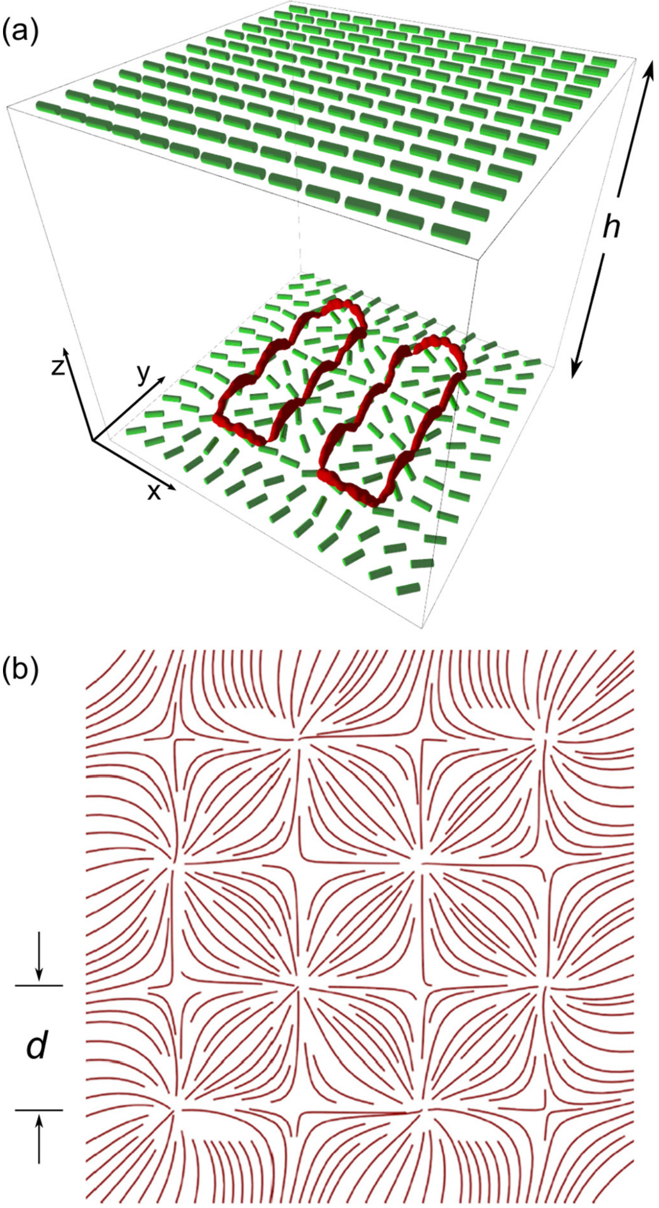

FIG. 2. Geometry and topology used in experimental and most numerical studies. (a) Nematic LC is confined to a plane-parallel cell. The bottom master plate strongly enforces a 4 × 4 array of $s = \pm 1$ surface defects as shown in (b). The top slave plate enforces isotropic tangential anchoring.

This is the solution to Laplace's equation that is appropriate in the equal elastic constant approximation [30]. Here, ϕ corresponds to the azimuthal orientation of the enforced nematic director field with respect to the x axis and k corresponds to the index of the N defects. We impose a "winding number-neutral" 4 × 4 grid ($N = 16$) of $s = \pm 1$ defects ($\sum_k s_k = 0$) with lattice spacing d in both the x and y directions. The opposing slave substrate enforces planar degenerate anchoring in which the director lies in the xy plane but is free to assume any orientation imposed elastically through the liquid crystal by the master surface. Furthermore, we allow the presence of a spatially homogeneous external electric field $\boldsymbol{E}$, which is applied either along the x or y direction, and we consider LCs with positive electric anisotropy [7].

III. MODELLING

A. Free energy

We used a Landau-de Gennes mesoscopic approach [7] in which nematic orientational order is modelled by the traceless and symmetric tensor nematic order parameter field $\boldsymbol{Q} = \sum_{i=1}^{3} \lambda_i(\boldsymbol{e}_i \otimes \boldsymbol{e}_i)$, where $\boldsymbol{e}_i$ are the eigenvectors and λ_i the corresponding eigenvalues. We considered LCs that exhibit equilibrium nematic uniaxial order, commonly expressed [7] as $\boldsymbol{Q}^{(u)} = S(\boldsymbol{n} \otimes \boldsymbol{n} - \frac{1}{3}\boldsymbol{I})$. Here, $S \in [-1/2, 1]$ stands for the uniaxial order parameter, the unit vector field $\boldsymbol{n}$ is referred to as the nematic director field, and $\boldsymbol{I}$ is the unit tensor.

We assume that the spatiotemporal evolution of the nematic order is determined by [31] $\gamma \frac{d\boldsymbol{Q}}{dt} = -\frac{\delta F}{\delta \boldsymbol{Q}}$, where the LC viscous properties are approximated by a single material parameter γ. We write the free energy $F = \int f d^3 r$ as the integral over the nematic LC confined within a plane-parallel cell of thickness h. The free energy $f = f_c + f_e + f_f$ consists of the condensation (f_c), elastic (f_e), and external field (f_f) contribution, which we express [7] as

$$f_c = \frac{1}{2}A_0(T - T^*)\mathrm{Tr}\boldsymbol{Q}^2 - \frac{1}{3}B\,\mathrm{Tr}\boldsymbol{Q}^3 + \frac{1}{4}C(\mathrm{Tr}\boldsymbol{Q}^2)^2, \quad (2a)$$

$$f_e = \frac{1}{2}L|\nabla \boldsymbol{Q}|^2, \quad (2b)$$

$$f_f = -\frac{1}{2}\varepsilon_0 \Delta\varepsilon E^2\, \boldsymbol{e}_E \cdot \boldsymbol{Q}\boldsymbol{e}_E. \quad (2c)$$

Here, A_0, B, and C are material constants, T^* is the supercooling temperature of the isotropic phase, L is the representative elastic modulus in the single elastic constant approximation, $\boldsymbol{E} = E\boldsymbol{e}_E$ is the external electric field pointing along the unit vector $\boldsymbol{e}_E$, ε_0 is the permittivity of free space, and $\Delta\varepsilon$ is the anisotropy of the dielectric constant.

B. Parametrisation and scaling

In our simulations we use the following parametrization in the Cartesian coordinate frame defined by the unit vectors $(\boldsymbol{e}_x, \boldsymbol{e}_y, \boldsymbol{e}_z)$:

$$\boldsymbol{Q} = \begin{bmatrix} q_1 + q_2 & q_3 & q_4 \\ q_3 & q_1 - q_2 & q_5 \\ q_4 & q_5 & -2q_1 \end{bmatrix}, \quad (3)$$

where q_1, q_2, q_3, q_4, and q_5 are variational parameters.

For scaling purposes we introduce [32] the dimensionless temperature $r = (T - T^*)/(T^{**} - T^*)$ and the scaled order parameter $\boldsymbol{Q} = \boldsymbol{Q}/S_0$, where $S_0 = \frac{B}{4C}$ and $T^{**} = T^* + B^2/(24A_0C)$ is the superheating temperature. We scale distances with respect to h, and measure the time with respect to the characteristic order parameter relaxation time $\tau = \frac{2\gamma}{3A_0(T^{**} - T^*)}$ expressed at $T = T^{**}$.

The resulting dimensionless free energy densities $\tilde{f}_c$, $\tilde{f}_e$, and $\tilde{f}_f$ can be expressed as

$$\tilde{f}_c = \frac{r}{6}\mathrm{Tr}\boldsymbol{Q}^2 - \frac{2}{3}\boldsymbol{Q}^3 + \frac{1}{8}(\boldsymbol{Q}^2)^2, \tag{4a}$$

$$\tilde{f}_e = \left(\frac{\xi_b}{h}\right)^2 |\tilde{\nabla}\boldsymbol{Q}|^2, \tag{4b}$$

$$\tilde{f}_f = -\left(\frac{\xi_b}{\xi_E}\right)^2 \boldsymbol{e}_E \cdot \boldsymbol{Q}\boldsymbol{e}_E. \tag{4c}$$

Here, $\xi_b = 2\sqrt{LC}/B$ is the bare biaxial correlation length [32], $\xi_E = \sqrt{LS_0/(\varepsilon_0 \Delta\varepsilon E^2)}$ is the external field extrapolation length [7,32] expressed at $T = T^{**}$, and $\tilde{\nabla} = h\nabla$.

Minimization of the free energy is performed numerically deep inside the nematic phase. At the master plate we enforce strong anchoring of the 4×4 pattern of $s = \pm 1$ defects using Eq. (1); at the slave plate we enforce strong degenerate planar anchoring, and use free boundary conditions at lateral walls. The corresponding interference textures are calculated for monochromatic light, with the polarizer and analyzer along $\boldsymbol{e}_x$ and $\boldsymbol{e}_y$, by using the Jones matrix beam propagation model [33], in which scattering and reflections are neglected.

We used the following parameters for simulations: $\frac{h}{\xi_b} = 50$, $\frac{d}{\xi_b} = 50$ (if not stated otherwise), $r = -8$. In calculating polarized microscopy textures, we impose crossed polarizers, and set $n_o = 1.54$ (ordinary refractive index), $n_e = 1.74$ (extraordinary index), $\lambda = 520$ nm (light wavelength), and $h = 16\ \mu$m.

IV. EXPERIMENTAL SETUP

For experiments we use the nematic liquid crystal 4-cyano-4′-pentylbiphenyl (5CB) confined to a cell of thickness $h = 16.0 \pm 0.2\ \mu$m. Our atomic force microscope (AFM) scribing method [25] is used to scribe the defect pattern given by Eq. (1) onto the polyvinyl alcohol coated master plate using an AFM stylus; here $d \sim 20\ \mu$m. The slave substrate is spin-coated with the planar-degenerate alignment layer polymethyl methacrylate.

The experiment requires two independent electric fields in the plane of the cell, each along one of the principle axes of the square array. To pattern the two electrode pairs, we mask four rectangular strips on an indium-tin-oxide (ITO) coated slide so that they form a square in the middle of the sample. The exposed ITO is removed by soaking in piranha solution, leaving behind two pairs of mutually orthogonal electrodes. A cartoon is shown in Fig. 3.

This ITO-coated master substrate is cleaned by sonicating sequentially in detergent, acetone, and ethanol, and then coated with the strong planar anchoring agent polyvinyl alcohol (PVA) by spin coating. The sample is baked at 170 °C for 2 h. We create a spatially varying easy axis over an $85 \times 85\ \mu$m square at the center of the electrode pattern by using a Bruker AFM stylus (TESPD, 300 kHz resonance) with a rigid cantilever (40 N/m spring constant) delivering a scribing force of about 1 μN, which does not measurably alter the PVA topography [25]. The scribing speed was approximately $18\ \mu\mathrm{m\,s}^{-1}$. AFM-scribed lines are spaced between 150 and 300 nm apart, with narrower spacings used in regions of higher curvature. The scribed region is shown pictorially by the small square in Fig. 3.

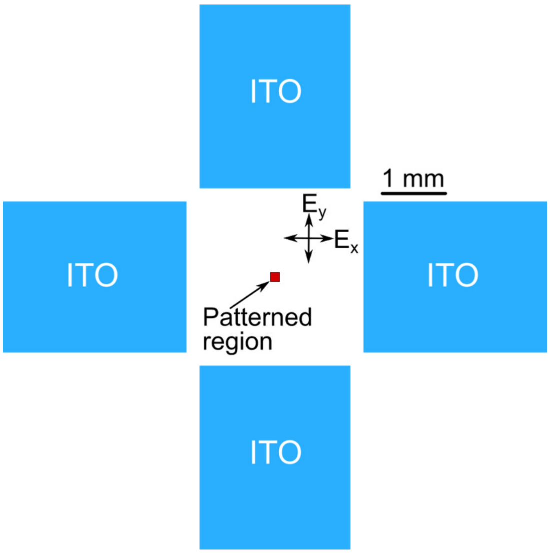

FIG. 3. Cartoon of master (patterned) surface. Two pairs of ITO electrodes are shown, allowing application of an electric field along the x axis or along the y axis. The patterned region is represented by the small square in the center. A scale bar is shown.

For the cell's opposing slave substrate, a glass slide was spin-coated with the planar-degenerate alignment layer [34] polymethyl methacrylate (PMMA) and baked at 80 °C for 2 h. On filling with liquid crystal, the initial alignment is isotropic planar, although a weak azimuthal memory effect develops over time. This memory effect is expected to have only a perturbative effect on the numerical simulations, which assume isotropic planar boundary conditions at the slave surface. A complete cell was assembled with Mylar spacers, and was measured by interferometry to have a thickness of $16.0 \pm 0.2\ \mu$m. The cell was filled with the positive dielectric anisotropy, room temperature nematic liquid crystal 4-cyano-4′-pentylbiphenyl (5CB) by capillary action in the isotropic phase. The sample was then cooled to the nematic phase and placed on the stage of a polarized microscope.

The ITO electrodes formed two pairs of orthogonal rectangles, with the shorter leg of each rectangle facing the patterned square. The gap along the x-axis electrode pair was $d_e^{(x)} = 2.35$ mm, and along the y axis it was $d_e^{(y)} = 2.59$ mm; both are much larger than the dimensions of the patterned square, and thus the field at the square can be considered uniform to better than 0.5%. For in-plane electrodes the applied electric field was determined by conformal mapping techniques, and is given at the midpoint between the electrodes by [35] $= \frac{2V}{\pi d_e}$, where V is the potential difference applied between electrodes. It is important to note that because of the positioning and small size of the scribed region as represented by the square in Fig. 3, and the fact that the cell thickness is much smaller than the gaps d_e, both the x and y electric fields are nearly uniform across the square and the z component of the electric field is virtually zero. We also remark that owing to the large electrode gaps d_e, ac voltages of many hundreds of volts were required (500 Hz square wave).

V. NUMERICAL SIMULATIONS

A. "Alphabet" of disclination patterns.

Of interest are different disclination patterns that could emerge from the master plate imposed 4 × 4 grid of surface defects in sufficiently thick cells ($h > d/2$). We first analyze the structure of disclinations and diversity of patterns that they form using the Landau-de Gennes mesoscopic [7] approach.

For conditions of interest (cells of thickness $h \sim 20\,\mu$m), each $s = \pm 1$ defect tends to decompose into a pair of half-integer daughter defects of the same total strength [see Fig. 1(b)]. This decomposition reduces the elastic energy, which scales as s^2 away from the defect core [7,36–38]. The decomposed daughter [39] defects repel each other such that, at the master surface, their separation distance is a competition between the anchoring strength imposed by the master substrate and the repulsion between same-strength defects (see Supplemental Material movie 1 in Ref. [40]).

For thin cells ($h \lesssim d/2$), disclination lines tend to be charged [41] and run from the positive (negative) defect at the master substrate to the induced defect of the same sign at the slave substrate. An example is shown in Fig. 4(a). However, for cells sufficiently thick relative to the defect d spacing, the disclination lines run approximately parallel to the patterned substrate, between defects having opposite strength [42,43]. These defects are chargeless, consisting of $s = +1/2$ and $s = -1/2$ sections, where a typical structure is depicted in Fig. 4(b). Running close to the master surface, these disclination lines are associated with the pair of daughter defects and are attracted by, and terminate on, nearest-neighbor defects of opposite sign. In the case of a single chargeless disclination, the director field far from the master surface tends to be aligned uniformly.

Possible stable and metastable patterns of chargeless disclinations generated by the master substrate imposed 4 × 4 array pattern of surface defects were obtained numerically in sufficiently thick cells ($h > d/2$) and are shown in Fig. 5. Each line defect connects a pair of nearest-neighbor daughter defects of opposite signs at the same master substrate. The resulting patterns form closed loops. Our geometry and topology allow an "alphabet" of 18 different patterns, exhibiting seven different symmetries. The seven disclination patterns, to which we refer as the *irreducible patterns*, are shown in the first and third rows of Fig. 5. All other patterns can be obtained from this set via rotations for an angle $\phi = N\frac{\pi}{2}$ around the z axis, where N is an integer. The top cell view is presented and disclinations are visualized by plotting regions of relatively strongly suppressed order parameter, which is realized in the cores of defects. The thickness of disclination lines is roughly given by the nematic biaxial correlation length [7,44] ξ_b. The corresponding calculated polarizing optical microscope images under crossed polarizers are given in the second and fourth panels of Fig. 5.

We henceforth label the irreducible set of disclination patterns as [II] [Fig. 5(a)], [U] [Fig. 5(b)], [O] [Fig. 5(c)], [oooo] [Fig. 5(d)], [Lo] [Fig. 5(e)], [Ioo] [Fig. 5(f)], and [H] [Fig. 5(g)], because these symbols roughly reflect key features of the patterns. Furthermore, for latter purpose we label the locations of $s = \pm 1$ surface defects at the master plate with a pair of indices $\{i,j\}$, where i and $j \in [1, 2, 3, 4]$ determine a row and column number of the 4 × 4 array. Here {1,1} and {4,4} locate the upper-left and bottom-right sides of the 4 × 4 checkerboard. Furthermore, we label by $\{i_1, j_1\} - \{i_2, j_2\}$ a disclination spanning the defect sites $\{i_1, j_1\}$ and $\{i_2, j_2\}$.

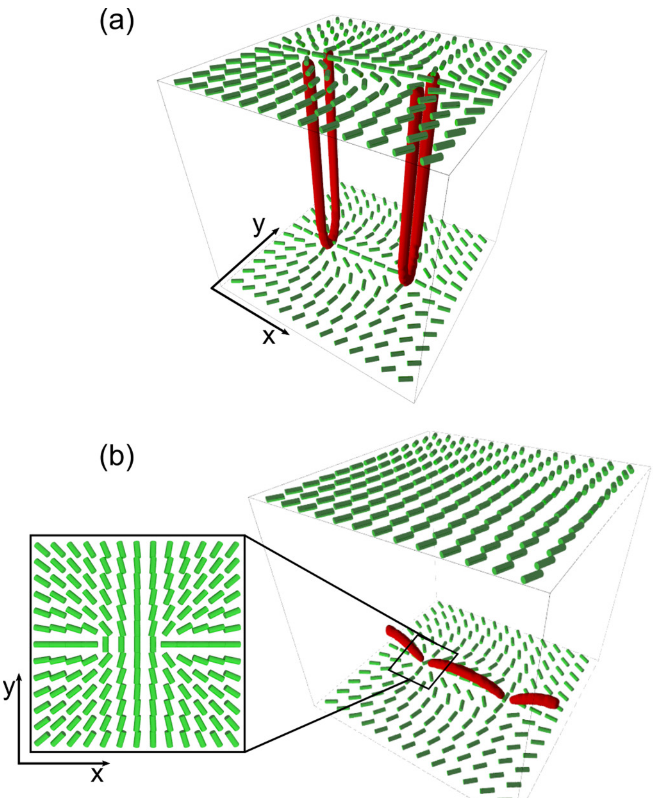

FIG. 4. Schematic sketches showing cells possessing either charged or chargeless line defects, where the master plate enforces $s = \pm 1$ surface point defects. (a) Charged $s = 1/2$ split disclination lines spanning the master and slave confining plate. (b) Chargeless line defects joining $s = \pm 1/2$ daughter defects within the master plate. Typical director field profiles are shown both just above the master plate and well above it. The red line indicates region where the amplitude $S = \sqrt{\frac{3}{2}\mathrm{Tr}\boldsymbol{Q}^2}$ of the order parameter $\boldsymbol{Q}$ is reduced to $S = S_{\mathrm{bulk}}/2$ due to strong local elastic distortions. Here, S_{bulk} stands for the bulk equilibrium value.

The free energies F of the patterns are, in general, different and depend on geometry and LC material properties. For example, for the set of parameters $\frac{h}{\xi_b} = \frac{d}{\xi_b} = 50$, a strong anchoring condition at the master plate and an absence of an external electric field, the excess free energy $\Delta F[\text{pattern}] = F - F_n$ of all patterns is roughly the same (their values differ for less than 1%), where F_n determines the free energy of the equilibrium bulk nematic. Only the free energy cost of the [H] structure is noticeably higher: $\frac{\Delta F[\mathrm{H}]}{\Delta F[\mathrm{II}]} \sim 1.01$. We used the configuration [II] as the reference pattern because it could be stabilized relatively simply.

To understand the switching mechanism among the competing patterns, it is instructive to visualize the typical nematic ordering of structures above the master plate, just below the average maximal height $z = z_{\max} \ll h$ of disclination lines.

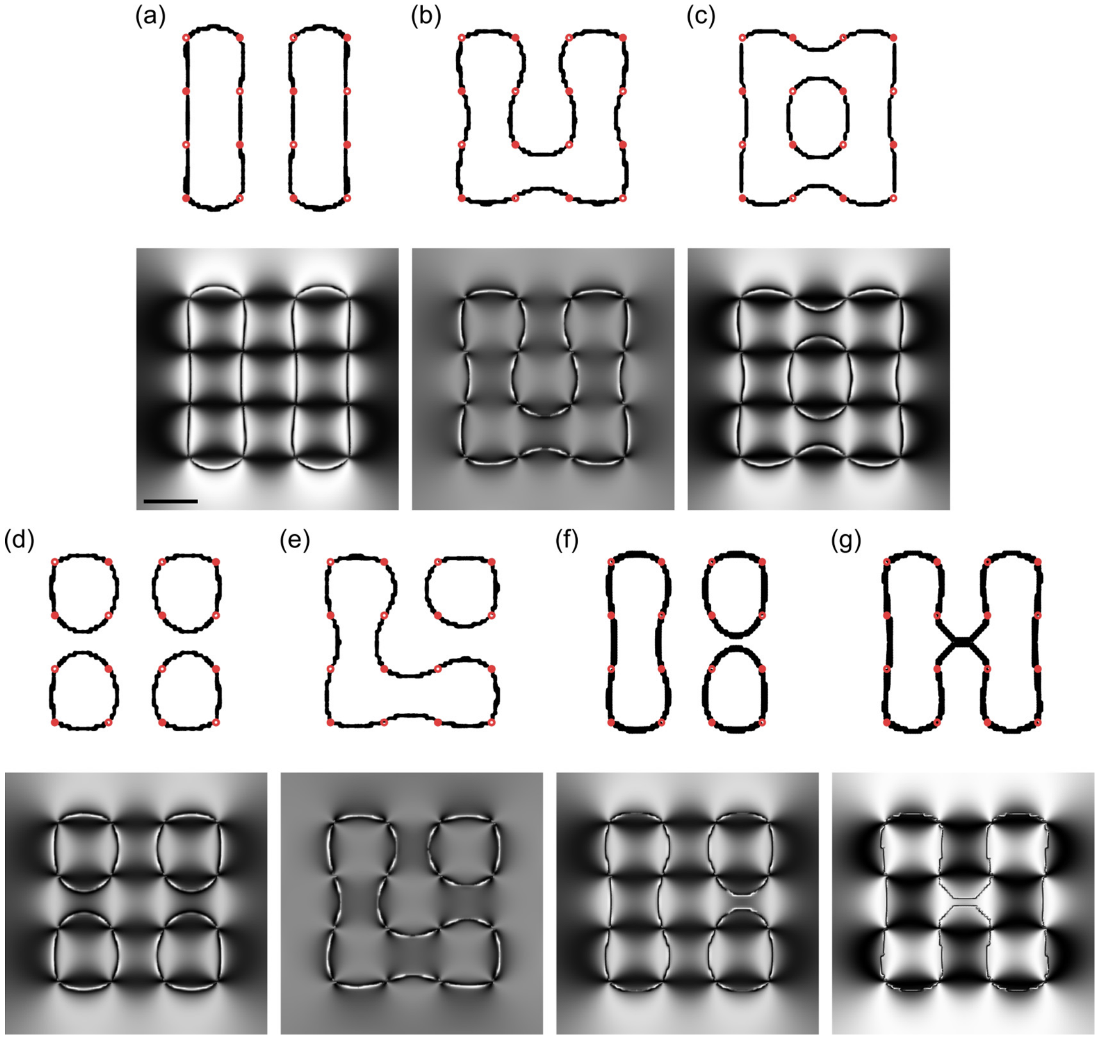

FIG. 5. Irreducible patterns. Numerically calculated nematic textures exhibiting seven different symmetries emerging from the enforced 4×4 array. The first and third rows: The top cell view of the line defect patterns where regions with strongly suppressed order parameter values are shown, fingerprinting the defect core regions. The solid and open circles indicate origins of nucleating $s = +1$ and $s = -1$ defect sites. The second and fourth rows: The corresponding typical optical microscopy textures obtained under crossed polarizers. Scale bar corresponds to the cell thickness h. From the *irreducible patterns,* one can generate an "alphabet" of 18 different patterns.

A representative example is presented in Fig. 6. Note that nematic orientational ordering is commonly represented by the nematic director field $\boldsymbol{n}$ for the orientational field in cases of uniaxial nematic ordering. However, close to disclinations the nematic order could enter biaxial states [44,45] due to relatively strong elastic distortions. Consequently, we plot the principal eigenvector $\boldsymbol{e}_1$ of $\boldsymbol{Q}$ corresponding to the largest $\boldsymbol{Q}$ eigenvalue. In cases of uniaxial order (which is strongly violated only within the cores of defects [45–47]) it holds that $\boldsymbol{e}_1 = \boldsymbol{n}$. Consequently, we henceforth refer to $\boldsymbol{e}_1$ as the nematic director field because the LC ordering is, in most parts of the sample, essentially uniaxial. In Fig. 6, we present the nematic director field of [II] within the (x,y) cross-sections at $z \sim z_{\max}$. Note that the master plate-imposed nematic pattern (at $z = 0$) is the same for all structures for strong enough anchoring and is schematically depicted in Fig. 2(b). The master surface enforces a zigzag domainlike pattern within the 4×4 checkerboard region, where the average orientation of neighboring domains tends to be oriented perpendicularly. Here each domain corresponds roughly to a region enclosed by four $s = \pm 1$ surface imposed defects. The master plate-enforced nematic structure, which is determined by Eq. (1), does not impose any preferred orientation. Note that in the case of charged disclinations, spanning the master and slave plates, this symmetry would be preserved on increasing z. However, confined chargeless disclinations break this symmetry, as illustrated in Fig. 6. The figure evidences a domain-type pattern, that dominates in the region $0 < z < z_{\max}$. For visualization purposes we also superimposed the pattern of line disclinations. One sees that the nematic structure surrounding a line connecting two neighboring surface defects—these lines also roughly match domain boundaries—is significantly different if the defects are connected, or not, by a disclination. In the former case, $\boldsymbol{e}_1$ reorients by $\pi/2$ on crossing domain boundaries (e.g., see the region enclosing the line [1,1]-[1,2] or [1,1]-[2,1]). This relatively abrupt reorientation is enabled via the order reconstruction mechanism [44,45]. On the contrary, in the latter case the principal field is more gradual (e.g., see

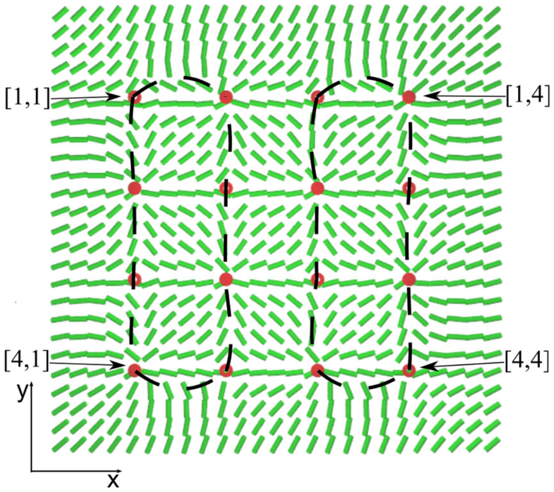

FIG. 6. Orientational field of the nematic structure shown in Fig. 5(a) just above the master plate. The (x,y) projection of the disclination pattern is superimposed with dotted lines. Positions of surface-enforced defects $s = \pm 1$ are marked with closed $(s = 1)$ and open $(s = -1)$ circles. Furthermore, positions of top-left ([1,1]), top-right ([1,4]), bottom-left ([4,1]), and bottom-right ([4,4]) surface defects are indicated. Note that the director profile reorients roughly by $\pi/2$ radians on crossing at right angles a disclination line position. On the other hand, transitions along boundaries of other domains are realized via a gradual splaylike reorientation.

the region enclosing the line [2,1]-[2,2]). Therefore confined disclinations introduce an anisotropic domain pattern, which is on average more responsive to imposed changes, e.g., via an external electric field. Furthermore, on increasing z above $z_{\max}$ nematic patterns progressively become homogeneously aligned along a symmetry breaking direction that lies within the (x,y) plane.

B. Pattern rewiring

One can realize transformations between different disclination patterns by rewiring just few pairs of facing disclinations into perpendicular directions. For example, this could be achieved efficiently by the use of laser tweezers [5] or by applying an appropriate external electric field $\boldsymbol{E}$.

In Fig. 7, we schematically sketch how all members of the irreducible set could be reached starting from [II] by rewiring just one or two pairs of facing disclinations. The pattern [II] could be obtained by imposing first a strong enough spatially homogeneous external electric field $\boldsymbol{E}$ along the x direction. After the desired pattern is formed, the field is switched off, while the structure remains trapped in one of the (meta) stable states. In Fig. 7, above the arrows, we schematically sketch the spatial profile of $\boldsymbol{E}$, which enables realisation of the displayed transformations. This is also the route that we used to obtain the remaining representative members of the irreducible set when starting from [II]. Note that all patterns are found to remain stable after the transformation-enabling $\boldsymbol{E}$ is switched off.

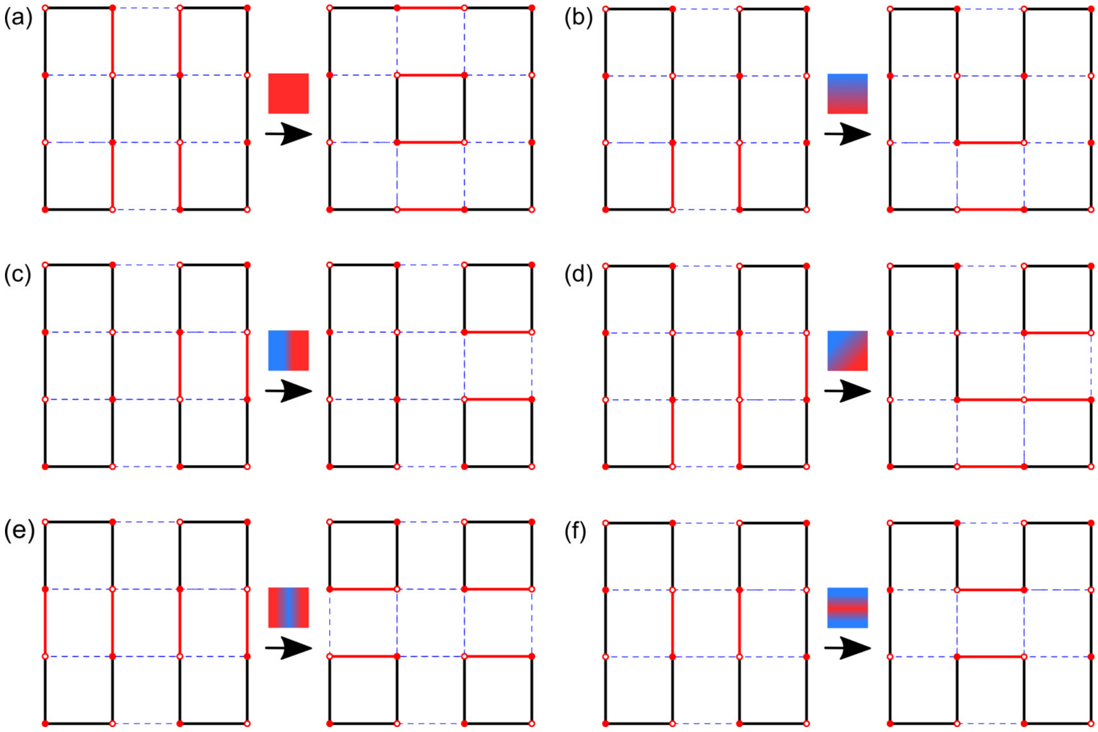

FIG. 7. Schematic representation of rewiring between different irreducible patterns. (a) [II]→ [O], (b) [II]→ [U], (c) [II]→ [Ioo], (d) [II]→ [Lo], (e) [II]→ [oooo], and (f) [II]→ [H]. Disclinations marked in red are rewired in the transformation. This may be accomplished, for example, by using a spatially dependent electric field: in the colored squares above the arrows, we schematically indicate the external electric field $\boldsymbol{E}$ spatial profile. Red and blue colors mark a relatively large and zero value of E, respectively. The diffuse regions correspond to spatially slow variation of field $\boldsymbol{E}$; the sharp transitions between red and blue correspond to a spatially rapid variation of $\boldsymbol{E}$. Note that for all cases only the pairs of facing disclinations need to be rewired.

The patterns [U], [Ioo], and [H] are realized by rewiring a single pair of facing disclinations when starting from [II]. However, one could also realize the other patterns (i.e., [O], [Lo], and [oooo]) by manipulating only one pair of disclinations by using a different initial pattern. For example, starting from [U] one could reach[O] by rewiring {1,2}-{2,2} and {1,3}-{2,3} into new pairs {1,2}-{1,3} and {2,2}-{2,3}. Furthermore, from [U] one gets [Lo] by rewiring the pairs {2,3}-{3,3} and {2,4}-{3,4} into {2,3}-{2,4} and {3,3}-{3,4}. Finally, [oooo] could be obtained from [Ioo] by rewiring {2,1}-{3,1} and {2,2}-{3,2} into {2,1}-{2,2} and {3,1}-{3,2}.

C. Rewiring mechanism

To realize electric field driven rewiring, we focus on the characteristic nematic director pattern above a chargeless disclination shown in Fig. 4(b). One sees that above the disclination line the director field tends to orient on average perpendicular to the disclination line's direction. Therefore, if $\boldsymbol{E}$ is applied parallel to the in-plane projection of the disclination lines, it tends to reorient the nematic director field along the electric field orientation for a positive dielectric anisotropy liquid crystal. This realignment can trigger reorientation of the disclination line for appropriate boundary conditions.

The tendency to realign a chargeless disclination line perpendicular to $\boldsymbol{E}$ is evident also from a simple free energy cost analysis of a straight disclination within a cylinder, where details are given in Appendix A. We use an ansatz for a straight chargeless disclination representing a possible solution in the equal elastic constant approximation of the Frank-Oseen continuum description [7], which we confine within a cylindrical volume. One sees (Appendix A) that the external electric field free energy contribution is minimum if the disclination direction and $\boldsymbol{E}$ are mutually perpendicular.

D. Rewiring a pair of disclinations

To demonstrate numerically the rewiring mechanism, we first consider the simplest possible arrangement of chargeless disclinations typifying a basic unit of our 4 × 4 template. For this purpose, we analyze $\boldsymbol{E}$-driven rewiring of a pair of chargeless disclinations (see Fig. 8) which are enabled by a master plate that enforces a 2 × 2 square array consisting of $s = \pm 1/2$ surface defects. (Note that all the defect sites would be connected by disclination lines for the case of a 2 × 2 array of $s = \pm 1$ surface defects.) In the initial configuration the disclination lines run along the x-axis. Then we apply a spatially homogeneous external field $\boldsymbol{E} = E\boldsymbol{e}_x$ and gradually increase its amplitude. We quantify the extent of the average nematic alignment along $\boldsymbol{E}$ with the quantity $S^{(x)} = \langle P_2(\boldsymbol{n} \cdot \boldsymbol{e}_x)\rangle$. Here, P_2 is the Legendre polynomial of order 2 and $\langle \ldots \rangle$ stands for the spatial average over the liquid crystal. For a spatially homogeneous nematic alignment along $\boldsymbol{E}$ it holds that $S^{(x)} = 1$; for an isotropic distribution of $\boldsymbol{n}$, $S^{(x)} = 0$. In Fig. 8(d), we demonstrate that $S^{(x)}$ on average increases on increasing E and $S^{(x)}$ saturates after the critical value of E triggering the rewiring is reached. The corresponding typical textures simulating polarizing microscopy experiment are shown in Supplemental Material movie 2 in Ref. [40].

We next demonstrate that a pair of parallel disclinations exhibit the attractive interaction, which in general moves the disclinations to bring them close. Let us consider the disclination pattern shown in Fig. 8(a) for $E = 0$. Initially, the surface defects are separated for distances $d_x = d_y = d$ in x and y directions, respectively. Note that the two disclinations are "antiparallel," the first one joining ($s = 1/2$ and $-1/2$) and the second one ($s = -1/2$ and $1/2$) nucleation surface defects, respectively. Therefore each segment of the first line faces a segment of the second line bearing the opposite signed winding number. Consequently, the lines attract each other, which causes their distortion shown in Fig. 9(b). In Fig. 9 (see also Supplemental Material movie 3 in Ref. [40]), we show that on gradually decreasing d_y and the attractive interaction could trigger the rewiring of disclinations. One sees that at a critical value of d_y the interacting lines collide and rewire in the y direction. The latter configuration is energetically more favorable than the previous one because of shorter total length of energetically costly disclinations.

E. Electric field driven rewiring between two different II patterns

Finally, we consider electric field driven rewiring realized in the geometry depicted in Fig. 2, where we use as the starting structure the pattern [II], oriented along the x direction. Note that from this reference pattern one could obtain the other structures using an appropriate $\boldsymbol{E}$ configuration, as shown in Fig. 7.

For a demonstrative rewiring example, we switch theoretically between two different realizations of the pattern [II], where as an intermediate state also the pattern [O] emerges [see Fig. 5(c)]. Representative rewiring stages are plotted in Fig. 10 (see also Supplemental Material movie 4 in Ref. [40]). In the initial state, the two loops characterizing the pattern are aligned along the x direction; see Fig. 10(a). This state is obtained by cooling from the isotropic phase in presence of a spatially homogenous external field $\boldsymbol{E} = E\boldsymbol{e}_y$, which is then switched off. Then we apply a gradually increasing field $\boldsymbol{E} = E\boldsymbol{e}_x$ along the x direction. On increasing E the disclinations progressively become distorted in the (x,y) plane. A collision of the distorted facing disclination lines enables their reconfiguration. Above the threshold field $E = E_2$ the pattern of two loops oriented along the y direction is formed [Fig. 10(d)]. Note that in the intermediate stage [Fig. 10(c)], the pattern shown in Fig. 5(c) was realized at $E = E_1 < E_2$. Importantly, the configurations shown in Figs. 10(c) and 10(d) persists when the field is switched off after each of these states is reached; thus, we have a truly multistable system.

VI. EXPERIMENTAL PROOF-OF-CONCEPT

Using our experimental setup, we demonstrate that the rewiring mechanism which our simulations yield could be indeed realized experimentally. For this purpose, we stabilize the pattern [II] using the AFM scribing method. Then we switch the disclinations using an in-plane external electric field between two different realizations of [II], mimicking simulation results shown in Fig. 10 and Supplemental Material movie 4 in Ref. [40]. Below we describe experimental

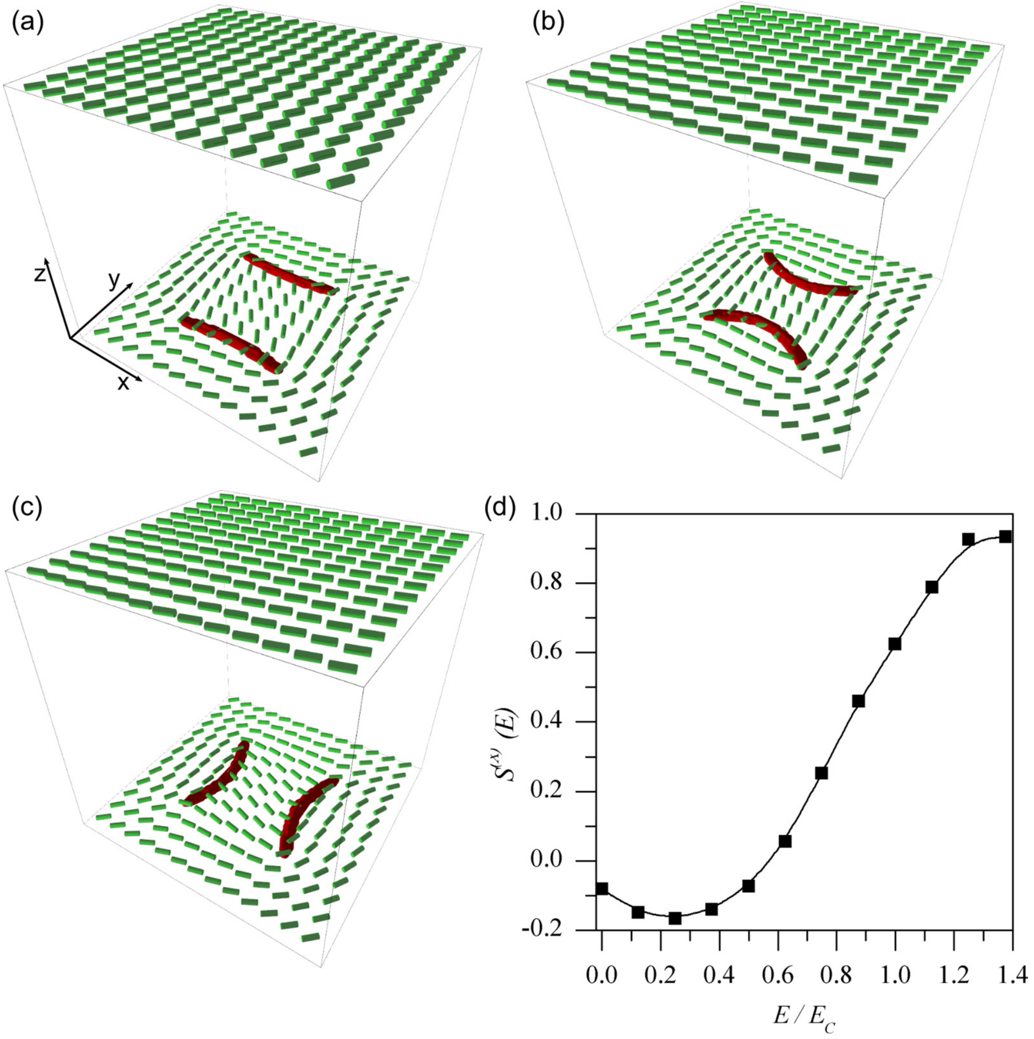

FIG. 8. Different stages of the electrical field driven rewiring mechanism shown for the case of a 2 × 2 array of $s = \pm 1/2$ master plate imposed defects. (a) $E = 0$, (b) $E \precsim E_c$ ($\xi_E = 1.118\,\xi_b$), (c) $E \succsim E_c$($\xi_E = 0.994\,\xi_b$). At $E = E_c$ (corresponding to $\xi_E \sim\ \xi_b$), the defect lines rewire. The nematic director field is plotted just above the master plate and at the slave plate, and we superimpose the line defect profile. (Points are plotted where the order parameter is strongly suppressed due to elastic distortions.) (d) $S^{(x)}(E)$ vs E/E_{c} is plotted. Calculated points are marked by square symbols and the line is the guide for an eye. Scale bar corresponds to the cell thickness h.

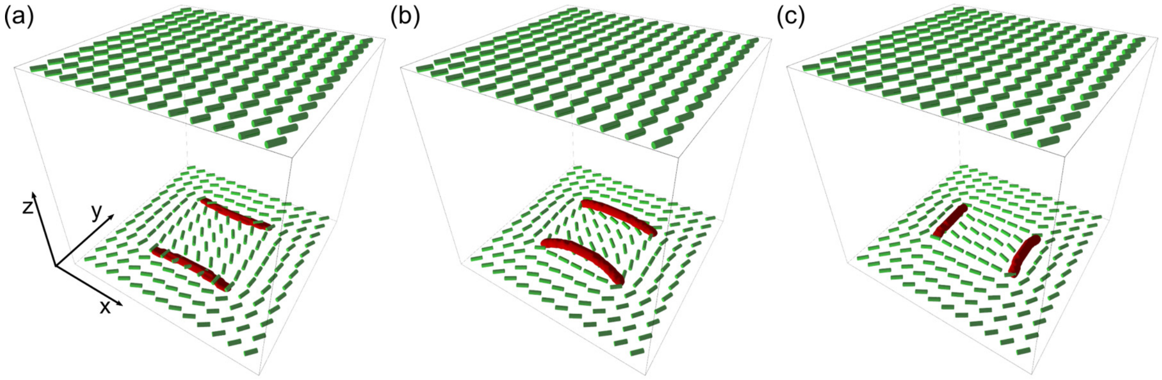

FIG. 9. Different stages of the thickness-driven rewiring mechanism shown for the case of a 2 × 2 array of $s = \pm 1/2$ master plate imposed surface defects. (a) $d_y/d_x = 1$, (b) 4/5, and (c) 3/5. The nematic director field is plotted just above the master plate and at the slave plate, and we superimpose the line defect profile. (Points are plotted where the order parameter is strongly suppressed due to elastic distortions.) Scale bar corresponds to the cell thickness h.

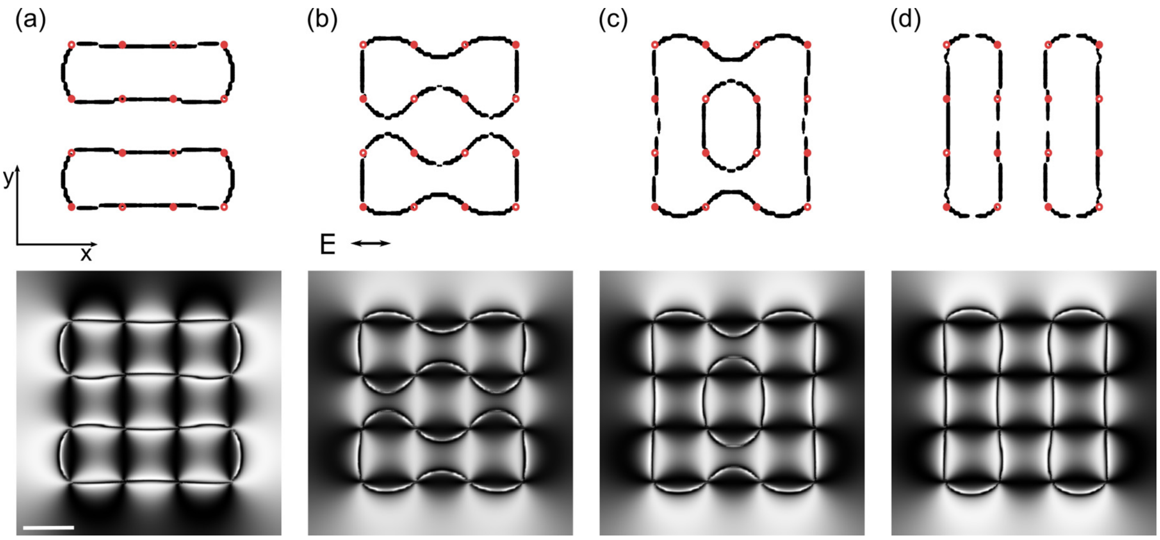

FIG. 10. Numerical simulation of the external electric field driven rewiring shown for the case of a 4 × 4 array of $s = \pm 1$ master plate imposed surface defects. Selected stages of the transition between two different realizations of structure depicted in Fig. 5(a) are shown. (Top rows) The top cell view of the line defect patterns where regions with strongly suppressed order parameter values are shown. (Bottom row) The corresponding *calculated* optical microscopy textures obtained under crossed polarizers. All structures and interference patterns were obtained numerically. In the simulation, we gradually increase E. (a) $\xi_b/\xi_E = 0$, (b) 1.12, (c) 1.23, and (d) 1.34. Scale bar corresponds to the cell thickness h.

measurements that confirm the predictive power and robustness of our simulation results.

We start from the pattern [II] aligned along the x direction. The applied voltage was increased at two very different rates to measure the threshold field(s), i.e., the electric field(s) at which the disclination lines can exchange termination partners and rotate by 90° in the xy plane. One method involved a slow quasiramp of the voltage along the x axis, from 0 to 633 V, in voltage steps of $\delta V_x = 2\,\mathrm{V}$, corresponding to field steps of $\delta E_x = 0.76\,\mathrm{kVm^{-1}}$, approximately every 5 seconds. A photomicrograph was taken at each step to record the position of the disclinations. When the ramp was completed, the process was repeated using a field along the y axis, with δE_y steps of $0.7\,\mathrm{kV\,m^{-1}}$. (The difference between δE_y and δE_y is due to a small anisotropy between the x and y electrode pairs.) A separate experiment was performed on the same sample in which the voltage (along the x axis) was increased quickly from 0 to a particular set voltage V_n over a timescale $<5\ \mu\mathrm{s}$, waiting 3 seconds, and then recording an image. The voltage then was returned to 0, allowing the distorted (but not yet rewired) defect lines to relax back to equilibrium. Some leftover distortion of the disclination lines is always present, so they were straightened to their initial configurations by applying a voltage along the y axis of 633 V for 3 seconds. The process was repeated, each time increasing the set voltage V_n in steps of $\delta V_x = 2.1\,\mathrm{V}$ until it reached a value for which all the segments had rewired. The entire experiment then was repeated for fields applied along the y axis. Importantly, disclinations that had been rewired at a particular set voltage V_n remained stable when the applied voltage was returned to zero; this demonstrates experimentally the multistability of the line defect patterns.

Due to the finite nature of the patterned array, there are three intermediate configurations for the experimentally observed cell that also are stable at zero field, and are accessible at intermediate field strengths, as seen in Figs. 11(c)–11(e). The threshold electric field at which the first intermediate configuration occurs is about 16% below the saturation field E_2, where the saturation field is the point at which the last defects exchange partners and further voltage increase has no effect. We found that all the defect lines exchanged termination partners at $E_2 = 135 \pm 10\,\mathrm{kV\,m^{-1}}$ in the x direction and $E_2 = 155 \pm 10\,\mathrm{kV\,m^{-1}}$ in the y direction when the voltage was increased quickly. When increasing the voltage slowly in steps of δE_x or δE_y, as appropriate, saturation was measured to be slightly smaller, viz. $E_2 = 125 \pm 10\,\mathrm{kV\,m^{-1}}$ in the x direction and $E_2 = 145 \pm 10\,\mathrm{kV\,m^{-1}}$ in the y direction. The discrepancies between the fast and slow voltage changes likely is due to the viscoelastic response time, indicating that the slow ramps were performed in equilibrium but the fast ramps were close to—but not quite in—equilibrium.

The discrepancies between the x and y saturation fields are likely due to detailed surface conditions, such as anisotropic anchoring due to the shape of the AFM stylus, or imperfections in the etched electrodes. In our experiment we used a pair of almost spatially homogenous electric fields E—one field (E_x) was oriented along the x axis and the other (E_y) along the y axis — to switch between the structures, where details are shown in Supplemental Material movie 5 [40].

The intermediate configurations are reproducible on repeated cycling of applied field. In Fig. 11(c), for example, the right-hand domain has been rewired. On symmetry grounds, the left-hand side could have been rewired first. In practice, small variations in the field and/or in the boundary conditions are sufficient to break the symmetry. Importantly, this symmetry-breaking could be exploited to create any desired sequence of rewiring by controlled AFM scribing (or alternatively, by selective ultraviolet light exposure [48,49]) to perturb appropriately a given part of the pattern.

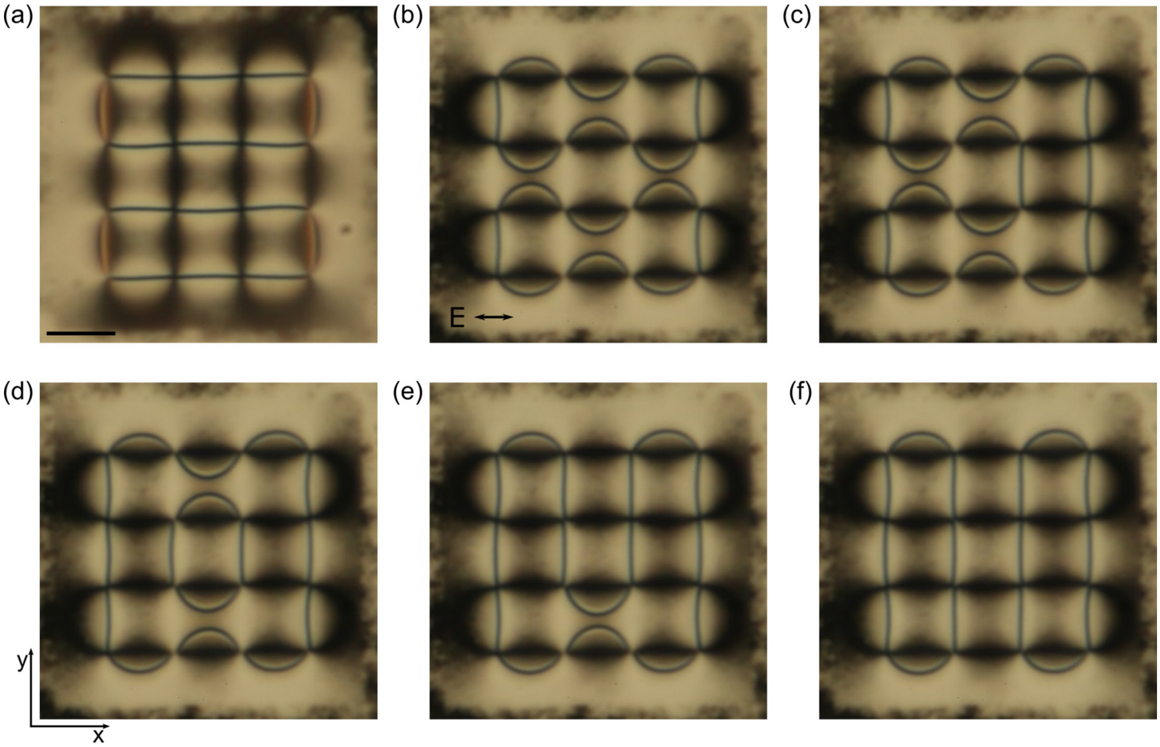

FIG. 11. Experimental observation of electric field driven rewiring of disclinations. A complete cell with a cell gap of $h = 16 \pm 0.2\,\mu$m. The cell is filled with the liquid crystal 5CB and imaged using a polarizing optical microscope, with the polarizer and analyzer oriented parallel and perpendicular to the image. (a) Photo taken at $E = 0$. The defects were previously aligned by applying a large field $\boldsymbol{E} = E\boldsymbol{e}_y$ in the y direction. (b) An ac electric field $\boldsymbol{E} = E\boldsymbol{e}_x$ is applied along the direction indicated, sufficiently large that the defect segments are close to osculating. (c)–(e) Intermediate defect configurations, each occurring successively with increasing $\boldsymbol{E} = E\boldsymbol{e}_x$. (f) Final configuration after the field has been increased above the critical field. All closed loop configurations remain stable when $\boldsymbol{E} = E\boldsymbol{e}_x$ is reduced to zero and can be switched back to configuration (a) by applying a sufficiently strong field $\boldsymbol{E} = E\boldsymbol{e}_y$ along the y axis. Scale bar in (a) corresponds to the surface defect distance $d \sim 20\,\mu$m.

Thus we clearly have switched experimentally between two different realizations [see Figs. 11(a) and 11(f)] of the theoretically predicted representative pattern shown in Fig. 5(a). Furthermore, the intermediate states depicted in Figs. 11(c) and 11(e) correspond to different realizations of the pattern in Fig. 5(b), and the experimental structure in Fig. 11(d) corresponds to that in Fig. 5(c). Each intermediate state is stable when the field at that point is switched to zero.

VII. CONCLUSIONS

We have demonstrated numerically and experimentally external electric field driven rewiring of a complex network of nematic line defects among competing configurations that are truly multistable, i.e., the new configurations survive even when the field is switched off. The set of available configurations was predetermined by a specific master surface nematic director field pattern. In our study the surface nematic director field at the master plate was fixed due to relatively strong boundary conditions. We switched between different patterns by rewiring disclinations close above the master plate using an appropriate external electric field configuration, which triggers molecular field changes in the sample. We illustrated the diversity of multistable and switchable configurations using an $N{\times}N$ array of charge ± 1 defects for $N = 4$. This is the simplest topologically neutral combination emerging from an $N{\times}N$ array of such defects, and provides complete proof-of-concept for this approach. Namely, $N = 2$ offers only a single pattern of disclinations, and $N = 3$ results in a net nonzero topological charge. For $N = 4$, we obtained 18 different patterns exhibiting seven different symmetries. By increasing N, the complexity of patterns would dramatically increase, although it would provide no additional physical insight into the phenomenon.

Our proof-of-principle study might pave the way for numerous applications, in particular in remotely addressable electrooptic, photonic, and emerging nanotechnological devices. Namely, different disclination patterns could enable different desired functionality of a system. For example, line defects could be exploited as efficient traps for appropriate nanoparticles [13,14,50]. These could introduce additional desired material properties into the system, e.g., electrical conductivity. In such a case, controlled and predetermined networks of these line defects would correspond to a complex network of conducting nano or micro wires with rewiring capability, where different configurations would correspond to different emergent functionalities.

Furthermore, these reconfigurable defects might provide insight into fundamental behaviors in Nature. If *fields* represent the fundamental entity of Nature [51], than topologically protected localized field distortions might represent fundamental particles, as first suggested by Skyrme [52]. In this view, we speculate that the fundamental understanding of chargeless lines in nematic LCs could yield some insight into intriguing Majorana particles [53], which behave simultaneously like matter and antimatter. Namely, our simulations reveal that an antiparallel pair of chargeless disclinations behave like a defect-antidefect pair. The facing segments of the defect lines exhibit opposite twisting and are mutually attractive if defects are sufficiently close, as shown in Fig. 9 and Supplemental Material movie 3 [40], thereby tending to annihilate each other. Note that a chargeless disclination of our study could be stable because its end-points are pinned to a confining substrate that enforces the surface defects. Therefore an unpinned chargeless loop would vanish with time by shrinking into a point, leaving nonsingular nematic ordering. However, our preliminary studies reveal that chargeless loops could be stabilized by toroidal topology [54,55], which will be the focus of future study.

ACKNOWLEDGMENTS

The authors acknowledge stimulating discussions with S. Žumer. This work was supported by the National Science Foundation Condensed Matter Physics Program (grants DMR1505389 and DMR1901797), the National Aeronautics and Space Administration (Grant NNX17AC76G), and by the Slovenian Research Agency (ARRS) under contracts P1-0099 and PR-07585.

APPENDIX: IMPACT OF AN EXTERNAL ELECTRIC FIELD ON DISCLINATIONS

Of interest is the impact of an external electric field $\boldsymbol{E}$ orientation on typical nematic disclinations. In our estimate, we use the Frank-Oseen continuum model [7] in which nematic structures are represented by the nematic director field $\boldsymbol{n}$. We use either Cartesian {x,y,z} or cylindrical coordinates $\{\rho, \varphi, z\}$, determined by unit vectors $\{\boldsymbol{e}_x, \boldsymbol{e}_y, \boldsymbol{e}_z\}$ and $\{\boldsymbol{e}_\rho, \boldsymbol{e}_\varphi, \boldsymbol{e}_z\}$, respectively. We consider straight disclinations running along the z axis.

The relevant free energy density terms $f = f_e + f_f$ consist of the elastic (f_e) and external field (f_f) contribution [7]:

$$f_e = \frac{K_1}{2}(\nabla\cdot\boldsymbol{n})^2 + \frac{K_2}{2}(\boldsymbol{n}\cdot\nabla\ \times\boldsymbol{n})^2 + \frac{K_3}{2}|\boldsymbol{n}\times\nabla\times\boldsymbol{n}|^2, \tag{A1a}$$

$$f_f = -\frac{S\,\varepsilon_0\Delta\varepsilon(\boldsymbol{E}\cdot\boldsymbol{n})^2}{2}, \tag{A1b}$$

where $\Delta\varepsilon$ is the field anisotropy and S stands for the uniaxial nematic order parameter. In the following, we use the approximation of equal Frank elastic constants $K \equiv K_1 = K_2 = K_3$, and express the external field in terms of the azimuthal (ϕ_E) and polar angle (θ_E) as

$$\boldsymbol{E} = E(\boldsymbol{e}_x\sin\theta_E\sin\phi_E + \boldsymbol{e}_y\sin\theta_E\cos\phi_E + \boldsymbol{e}_z\cos\theta_E). \tag{A2}$$

The solutions [7,20] of the relevant Euler-Lagrange equations, corresponding to charged and chargeless disclinations, can be expressed as

$$\boldsymbol{n} = \boldsymbol{e}_x\cos\theta + \boldsymbol{e}_y\sin\theta\cos\gamma + \boldsymbol{e}_z\sin\theta\sin\gamma. \tag{A3}$$

"Elementary" charged disclinations are determined by

$$\gamma = 0, \quad \theta = \pm\tfrac{1}{2}\arctan(y/x). \tag{A3a}$$

Furthermore, a representative chargeless disclination is described by

$$\gamma = \pi z/h_0, \quad \theta = 1/2\arctan(y/x). \tag{A3b}$$

Here, h_0 determines the distance, where the disclination switches between the "planar" $s = 1/2$ and $s = -1/2$ pattern. Therefore $\boldsymbol{n}(z=0) = \boldsymbol{e}_x\cos\theta + \boldsymbol{e}_y\sin\theta$ and $\boldsymbol{n}(z=h) = \boldsymbol{e}_x\cos\theta - \boldsymbol{e}_y\sin\theta$. Within this description the "out-of-plane" twist deformation of the disclination varies linearly with z. Note that charged and chargeless disclinations also can be called, respectively, as *wedge* and *twist* disclinations in the literature [7,20].

We use the ansatz Eq. (A3) to express the free energy penalties, where we confine disclinations within a cylinder of radius R:

$$g^{(w)} = \frac{1}{4\varrho^2} - \frac{\sin^2\theta_E}{2\xi_E^2}, \tag{A4a}$$

$$g^{(t)} = \frac{1}{\varrho^2} + \frac{\pi^2}{2h^2} + \frac{1}{\xi_E^2}\left(-\frac{5}{16} + \frac{\cos(2\theta_E)}{16} + \frac{\sin(2\theta_E)\sin\phi_E}{2\pi}\right), \tag{A4b}$$

where $g^{(\mathrm{dis})} = \frac{1}{Kh_0\pi}\iint_{0,0}^{h_0,2\pi} f\,dz\,d\varphi$ and the superscript "dis" labels either the wedge (w, that is, charged) or twist (t, that is, chargeless) disclination, and $\xi_E = \sqrt{K/(S\varepsilon_0\Delta\varepsilon E^2)}$ stands for the external electric field coherence length.

It follows that both kind of disclinations tend to be oriented perpendicular to $\boldsymbol{E}$ for $\Delta\varepsilon > 0$, namely,

$$g^{(w)}\left[\theta_E = \frac{\pi}{2}\right] - g^{(w)}[\theta_E = 0] = -\frac{1}{2\xi_E^2}, \tag{A5a}$$

$$g^{(t)}\left[\theta_E = \frac{\pi}{2}\right] - g^{(t)}[\theta_E = 0] = -\frac{1}{8\xi_E^2}. \tag{A5b}$$

[1] N. Mermin, The topological theory of defects in ordered media, Rev. Mod. Phys. **51**, 591 (1979).

[2] Y. Zhenwei and M. O. Cruz, Polydispersity-driven topological defects as order-restoring excitations, Proc. Natl. Acad. Sci. USA **111**, 5049 (2014).

[3] S. Zhou, S. V. Shiyanovskii, H. S. Park, and O. D. Lavrentovich, Fine structure of the topological defect cores studied for disclinations in lyotropic chromonic liquid crystals, Nat. Commun. **8**, 14974 (2017).

[4] A. Martinez, M. Ravnik, B. Lucero, R. Visvanathan, S. Žumer, and I. I. Smalyukh, Mutually tangled colloidal knots and induced defect loops in nematic fields, Nat. Mater. **13**, 258 (2014).

[5] M. Nikkhou, M. Škarabot, S. Čopar, M. Ravnik, S. Žumer, and I. Muševič, Light-controlled topological charge in a nematic liquid crystal, Nat. Phys. **11**, 183 (2015).

[6] P. M. Chesler, A. M. García-García, and H. Liu, Defect Formation Beyond Kibble-Zurek Mechanism and Holography, Phys. Rev. X **5**, 021015 (2015).

[7] P. G. De Gennes and J. Prost, *The Physics of Liquid Crystals* (Clarendon, Oxford, 1994).

[8] N. D. Mermin and T. I. Ho, Circulation and Angular Momentum in the A Phase of Superfluid Helium-3, Phys. Rev. Lett. **36**, 594 (1976).

[9] P. C. Hendry, N. S. Lawson, R. A. M. Lee, P. V. E. McClintock, and C. D. H. Williams, Generation of defects in superfluid ^{4}He as an analogue of the formation of cosmic strings, Nature (London) **368**, 315 (1994).

[10] C. N. Weiler, T. W. Neely, D. R. Scherer, A. S. Bradley, M. J. Davis, and B. P. Anderson, Spontaneous vortices in the formation of Bose-Einstein condensates, Nature (London) **455**, 948 (2008).

[11] A. A. Abrikosov, The magnetic properties of superconducting alloys, J. Phys. Chem. Sol. **2**, 199 (1957).

[12] L. Marrucci, C. Manzo, and D. Paparo, Optical Spin-to-Orbit Angular Momentum Conversion in Inhomogeneous Anisotropic Media, Phys. Rev. Lett. **96**, 163905 (2006).

[13] H. Kikuchi, M. Yokota, M. Hisakado, H. Yang, and T. Kajiyama, Polymer-stabilized liquid-crystals blue phases, Nat. Mater. **1**, 64 (2002).

[14] D. Coursault, J. Grand, B. Zappone, H. Ayeb, G. Levi, N. Félidj, and E. Lacaze, Linear self-assembly of nanoparticles within liquid crystal defect arrays, Adv. Mater. **24**, 1461 (2012).

[15] Q. Liu, Y. Chui, D. Gardner, X. Li, S. He, and I. I. Smalyukh, Self-alignment of plasmonic gold nanorods in reconfigurable anisotropic fluids for tunable bulk metamaterial applications, Nano Lett. **10**, 1347 (2010).

[16] E. Karatairi, B. Rožič, Z. Kutnjak, V. Tzitzios, G. Nounenis, G. Cordoyiannis, J. Thoen, C. Glorieux, and S. Kralj, Nanoparticle-induced widening of the temperature range of liquid-crystalline blue phases, Phys. Rev. E **81**, 041703 (2010).

[17] H. Yoshida, K. Asakura, J. Fukuda, and M. Ozaki, Three-dimensional positioning and control of colloidal objects utilizing engineered liquid crystalline networks, Nat. Commun. **6**, 7180 (2015).

[18] D. Pires, J. B. Fleury, and Y. Galerne, Colloid Particles in the Interaction Field of a Disclination Line in a Nematic Phase, Phys. Rev. Lett. **98**, 247801 (2007).

[19] M. V. Kurik and O. D. Lavrentovich, Defects in liquid crystals: homotopy theory and experimental studies, Usp. Fiz. Nauk **154**, 381 (1988) [Sov. Phys. Usp. **31**, 196 (1988)].

[20] S. Afghah, R. L. B. Selinger, and J. V. Selinger, Visualising the crossover between 3D and 2D topological defects in nematic liquid crystals, Liq. Cryst. **45**, 2022 (2018).

[21] P. E. Cladis and M. Kleman, Non-singular disclinations of strength $S = +1$ in nematics, J. Phys. **40**, 325 (1979).

[22] A. Nych, J. Fukuda, U. Ognysta, S. Žumer, and I. Muševic, Spontaneous formation and dynamics of half-skyrmions in a chiral liquid-crystal film, Nat. Phys. **13**, 1215 (2017).

[23] U. Tkalec, M. Ravnik, S. Čopar, S. Žumer, and I. Muševič, Reconfigurable knots and links in chiral nematic colloids, Science **333**, 62 (2011).

[24] Q. Liu, B. Senyuk, M. Tasinkevych, and I. I. Smalyukh, Nematic liquid crystal boojums with handles on colloidal handlebodies, Proc. Natl. Acad. Sci. USA **110**, 9231 (2013).

[25] B. S. Murray, R. A. Pelcovits, and C. Rosenblatt, Creating arbitrary arrays of two-dimensional topological defects, Phys. Rev. E **90**, 052501 (2014).

[26] J. S. B. Tai and I. I. Smalyukh, Three-dimensional crystals of adaptive knots, Science **365**, 1449 (2019).

[27] Y. Guo, M. Jiang, C. Peng, K. Sun, O. Yaroshchuk, O. Lavrentovich, and Q. H. Wei, High-resolution and high-throughput plasmonic photopatterning of complex molecular orientations in liquid crystals, Adv. Mater. **28**, 2353 (2016).

[28] Y. Sasaki, V. S. R. Jampani, C. Tanaka, N. Sakurai, S. Sakane, K. V. Le, F. Araoka, and H. Orihara, Large-scale self-organization of reconfigurable topological defect networks in nematic liquid crystals, Nat. Commun. **7**, 13238 (2016).

[29] J. S. Gwag, Y. K. Kim, C. H. Lee, and J. H. Kim, Realization of multi-stable ground states in a nematic liquid crystal by surface and electric field modification, Sci. Rep. **5**, 11368 (2015).

[30] J. Nehring and M. Saupe, On the schlieren texture in nematic and smectic liquid crystals, J. Chem. Soc., Faraday Trans. 2 **68**, 1 (1972).

[31] M. Ravnik and S. Žumer, Landau–de Gennes modelling of nematic liquid crystal colloids, Liq. Cryst. **36**, 1201 (2009).

[32] F. Bisi, E. C. Garland, R. Rosso, and E. G. Virga, Order reconstruction in frustrated nematic twist cells, Phys. Rev. E **68**, 021707 (2003).

[33] D. H. Goldstein, *Polarized Light*, 3rd ed. (CRC Press, Boca Raton, 2010).

[34] I. M. Syed, G. Carbone, C. Rosenblatt, and B. J. Wen, Planar degenerate substrate for micro- and nanopatterned nematic liquid crystals, Appl. Phys. **98**, 034303 (2005).

[35] C. Rosenblatt, R. B. Meyer, R. Pindak, and N. A. Clark, Temperature behavior of ferroelectric liquid crystal thin films, Phys. Rev. A **21**, 140 (1980).

[36] D. Svenšek and S. Žumer, Instability modes of high-strength disclinations in nematics, Phys. Rev. E **70**, 061707 (2004).

[37] R. Stannarius and K. Harth, Defect Interactions in Anisotropic Two-Dimensional Fluids, Phys. Rev. Lett. **117**, 157801 (2016).

[38] S. Kralj, B. S. Murray, and C. Rosenblatt, Decomposition of strongly charged topological defects, Phys. Rev. E **95**, 042702 (2017).

[39] B. S. Murray, S. Kralj, and C. Rosenblatt, Decomposition vs. escape of topological defects in a nematic liquid crystal, Soft Matter **13**, 8442 (2017).

[40] See Supplemental Material at http://link.aps.org/supplemental/10.1103/PhysRevResearch.2.013176 for movies showing the simulated impact of cell thickness on line defect structure, simulated electric and distance driven rewiring of a patterned 2×2 cell, and simulated and experimental electric field driven rewiring of a 4×4 patterned cell.

[41] C. Chiccoli, I. Feruli, O. D. Lavrentovich, P. Pasini, S. V. Shiyanovskii, and C. Zannoni, Topological defects in schlieren textures of biaxial and uniaxial nematics, Phys. Rev. E **66**, 030701 (2002).

[42] A. S. Backer, A. C. Callan-Jones, and R. A. Pelcovits, Nematic cells with defect-patterned alignment layers, Phys. Rev. E **77**, 021701 (2008).

[43] M. Ambrožič and S. Kralj, Thickness induced line-defect reconfigurations in thin nematic cell, Adv. Cond. Mat. Phys. **2019**, 4256526 (2019).

[44] R. Hamdi, G. Lombardo, M. P. Santo, and R. Barberi, Biaxial coherence length in a nematic π-cell, Eur. Phys. J. E **36**, 115 (2013).

[45] N. Schopohl and T. J. Sluckin, Defect Core Structure in Nematic Liquid Crystals, Phys. Rev. Lett. **59**, 2582 (1987).

[46] S. Kralj and E. G. Virga, Universal fine structure of nematic hedgehogs, J. Phys. A **34**, 829 (2001).

[47] T. Bellini, M. Buscaglia, C. Chiccoli, F. Mantegazza, P. Pasini, and C. Zannoni, Nematic with Quenched Disorder: How Long Will It Take to Heal? Phys. Rev. Lett. **88**, 245506 (2002).

[48] T. Shioda, B. Wen, and C. Rosenblatt, Step-wise Fréedericksz transition in a nematic liquid crystal, J. Appl. Phys. **94**, 7502 (2003).

[49] K. V. Vaughn, M. Sousa, D. Kang, and C. Rosenblatt, Continuous control of liquid crystal pretilt angle from homeotropic to planar, Appl. Phys. Lett. **90**, 194102 (2007).

[50] X. Wang, D. S. Miller, E. Bukusoglu, J. J. De Pablo, and N. L. Abbott, Topological defects in liquid crystals as templates for molecular self-assembly, Nat. Mater. **15**, 106 (2016).

[51] A. Hobson, There are no particles, there are only fields, Am. J. Phys. **81**, 211 (2013).

[52] T. Skyrme, A unified field theory of mesons and baryons, Nucl. Phys. **31**, 556 (1962).

[53] F. Wilczek, Majorana returns, Nat. Phys. **5**, 614 (2009).

[54] M. Bowick, D. R. Nelson, and A. Travesset, Curvature-induced defect unbinding in toroidal geometries, Phys. Rev. E **69**, 041102 (2004).

[55] D. Jesenek, S. Kralj, R. Rosso, and E. G. Virga, Defect unbinding on a toroidal nematic shell, Soft Matter **11**, 2434 (2015).